

# Limits of isotropic damage models for complex load paths — beyond stress triaxiality and Lode angle parameter

K. Feike, P. Kurzeja, J. Mosler, K. Langenfeld\*

*TU Dortmund University, Institute of Mechanics, Leonhard-Euler-Str. 5, D-44227 Dortmund, Germany*

---

## Abstract

The stress triaxiality and the Lode angle parameter are two well established stress invariants for the characterization of damage evolution. This work assesses the limits of this tuple by using it for damage predictions via ductile damage models from continuum damage mechanics. Isotropic and anisotropic formulations of two well-established models are used to avoid model-specific restrictions. The damage evolution is analyzed for different load paths, while the stress triaxiality and the Lode angle parameter are controlled. The equivalent plastic strain is moreover added as a third parameter. These analyses reveal that this triple does still not suffice to uniquely define the damage state. As a consequence, well-established concepts such as fracture surfaces depending on this triple have to be taken with care, if complex paths are to be investigated. These include, e.g., load paths observed during metal forming applications with varying load directions or multiple stages.

*Keywords:* damage, triaxiality, lode angle, path dependence

---

## 1. Introduction

The prediction of damage in materials is still a major challenge in many engineering disciplines since the underlying mechanisms are even nowadays not fully understood. As a result, large safety factors are mandatory to statistically ensure the functionality of structures and components. The modeling of the underlying material behavior is thus a key aspect for understanding and predicting the performance of these parts, cf. [1, 2, 3].

From a microscopic view, the mechanism of ductile damage can be related to the nucleation, the growth and finally the coalescence of voids induced by plastic deformation [4]. Depending on the material of interest, voids can show different origins and shapes, e.g., decohesion at hard particles. Since voids reduce the effective (load-carrying) area, they result in a reduced effective material stiffness [5], which ultimately also reduces the load-bearing capacity of the material. A natural modeling framework is thus the effective stress concept, cf. [6, 7]. Within this concept, which is also known as principle of strain equivalence, the true stresses are introduced. They are defined with respect to the effective cross sectional area caused by void nucleation, growth and coalescence. An alternative modeling concept is based on effective strains, which can be interpreted as the decomposition of the total strains into elastic and damage-related parts [8, 9]. Finally, an effective damage-induced elastic stiffness can also be derived by means of the concept of strain energy equivalence [10, 11]. In contrast to the concept of effective stresses and the concept of effective strains, the variational principle of strain energy equivalence naturally enforces physically relevant invariances. For instance, it naturally leads to a symmetric Cauchy stress even for anisotropic damage degradation (certainly, provided a Boltzmann continuum is considered).

---

\*Corresponding author. kai.langenfeld@tu-dortmund.de

Turning the view to the macroscopic description, a common approach for damage characterization is based on stress invariants like triaxiality  $\eta$  and Lode angle parameter  $\bar{\theta}$

$$\eta = \frac{\sqrt{2}}{3} \frac{\sigma_1 + \sigma_2 + \sigma_3}{[\sigma_1 - \sigma_2]^2 + [\sigma_2 - \sigma_3]^2 + [\sigma_3 - \sigma_1]^2} \quad (1)$$

$$\bar{\theta} = 1 - \frac{2}{\pi} \arccos\left(\frac{L [L - 3] [L + 3]}{[L^2 + 3]^{3/2}}\right) \quad \text{with} \quad L = \frac{2\sigma_2 - \sigma_1 - \sigma_3}{\sigma_3 - \sigma_1} \quad (2)$$

combined with an equivalent plastic strain, cf. [12, 13], via

$$\varepsilon^{\text{p,eq}} = \int \sqrt{\frac{2}{3} \dot{\varepsilon}^{\text{p}} : \dot{\varepsilon}^{\text{p}}} dt. \quad (3)$$

Value  $L$  is the Lode parameter and  $\sigma_i$  the stress eigenvalues. Moreover,  $\dot{\varepsilon}^{\text{p}}$  corresponds to the plastic strain rate tensor. From a mathematical point of view the aforementioned characterization corresponds to an isotropic approximation. Early research showed that the stress triaxiality can be related to the physical process of void nucleation, growth and coalescence, cf. [14, 15]. Likewise, the Lode angle parameter was found to characterize damage evolution at low stress triaxialities, see [13]. More recently, the Lode angle parameter has been investigated for different fracture criteria in order to characterize the onset of damage [16]. Additional influences of the complete stress state on the damage evolution are often not considered, for instance, those accounting for anisotropic behavior. Moreover, the triple of stress triaxiality, Lode angle parameter and equivalent plastic strain often changes in time for complex load paths. Therefore, such load paths – as occurring in forming processes [17] – require an extended description. The present work thus analyzes the limits of simplified isotropic damage characterizations such as that given by Eqs. (1)–(3) and identifies suitable and unsuitable load conditions.

The focus of this work is on ductile damage in the context of continuum damage mechanics. The key highlights are:

- The frequently applied recommendation ”the lower the stress triaxiality, the lower the damage accumulation” is shown to be wrong for certain complex load paths.
- Such load paths are identified by means of computational optimization.
- An improved characterization of damage by means of the stress triaxiality, the Lode (angle) parameter as well as the equivalent plastic strains, as employed in the concept of fracture surfaces [13], is shown to be still insufficient.
- Finally, even a characterization of damage by a complete isotropic representation of the stress tensor (all invariants) is demonstrated to be inaccurate for complex load paths.

In order to elaborate these highlights, two general anisotropic damage models depending on the complete stress tensor are considered and subsequently simplified in a controlled manner. For instance, the prediction capabilities of the models for two different load paths with identical stress triaxialities and/or Lode angle parameters are compared. Since such numerical experiments may also depend on the underlying constitutive model, two different modeling frameworks are adopted. While the first is based on the principle of energy equivalence [10, 18, 11], the latter is the by now classic Lemaitre model [19].

This work is structured as follows. Section 2 describes two constitutive models based on continuum damage mechanics, which form the basis for the subsequent investigations. Numerical methods in order to discretize, control and optimize load paths are presented in Section 3. Particularly, techniques for prescribing the stress-triaxiality and the Lode (angle) parameter are presented. The main findings are reported in Section 4. It covers numerical experiments highlighting the limits of different isotropic damage characterizations.

## 2. Continuum damage mechanics – two prototype models

Two constitutive models are briefly presented for the prediction of ductile damage, both as isotropic and anisotropic formulations. This allows a comprehensive load path analysis that is not bound to the characteristics of a single model. The two models are characteristic prototypes of the effective configuration concept (also known by the principle of strain energy equivalence) and the effective stress concept (also known by the principle of strain equivalence). While model *ECC* is based on the principle of strain energy equivalence, model *LEM* (Lemaitre model) falls into the range of the principle of strain equivalence. All models are calibrated with the same experimental data and form the basis for the subsequent numerical investigations.

### 2.1. ECC-Model – Effective Configuration Concept

The first model is based on the concept of strain energy equivalence, cf. [10]. The constitutive relations are adopted from the works in [11, 18]. The Helmholtz energy  $\psi$  is additively decomposed into an elastic part ( $\psi^e$ ) and a plastic part ( $\psi^p$ ) according to

$$\psi = \psi^e(\boldsymbol{\varepsilon}, \boldsymbol{\varepsilon}^p, \mathbf{b}) + \psi^p(\mathbf{a}, \mathbf{k}, \mathbf{b}, \boldsymbol{\varepsilon}^p), \quad (4)$$

$$\psi^e = \frac{\lambda}{2} [\mathbf{b} : \boldsymbol{\varepsilon}_+^e + \mathbf{I} : \boldsymbol{\varepsilon}_-^e]^2 + \mu [\mathbf{b} : [\boldsymbol{\varepsilon}_+^e \cdot \mathbf{b} \cdot \boldsymbol{\varepsilon}_+^e] + \boldsymbol{\varepsilon}_-^e : \boldsymbol{\varepsilon}_-^e], \quad (5)$$

$$\psi^p = \frac{H_k}{2} [\mathbf{b} : \mathbf{k}]^2 + \frac{H_a}{2} \mathbf{b} : [\mathbf{a} \cdot \mathbf{b} \cdot \mathbf{a}]. \quad (6)$$

The strain tensor  $\boldsymbol{\varepsilon}$  is also additively decomposed into an elastic and a plastic part, i.e.,  $\boldsymbol{\varepsilon} = \boldsymbol{\varepsilon}^e + \boldsymbol{\varepsilon}^p$ , cf. [20]. The model captures isotropic as well as kinematic hardening due to the state variables  $\mathbf{k}$  and  $\mathbf{a}$ , respectively. Here, isotropic hardening is captured by a tensorial internal variable, following the principle of strain energy equivalence [11]. Both the elastic and the plastic energy contribution are affected by the damage evolution due to integrity tensor  $\mathbf{b}$ . The integrity tensor can be interpreted as an inverse damage measure, i.e.,  $\mathbf{b} = \mathbf{I}$  represents the virgin material, while some of the eigenvalues of  $\mathbf{b}$  converge to zero for completely damaged material points. By choosing  $\mathbf{b} = \mathbf{I}$ , Hooke's law is recovered. Accordingly,  $\lambda$  and  $\mu$  are the Lamé parameters. Furthermore,  $H_k$  is the isotropic hardening modulus and  $H_a$  is the kinematic hardening modulus.

A crucial contribution to the material model is the micro-closure-reopening (MCR) effect, which only allows damage evolution under tensile modes. Within the present model, the MCR effect is incorporated through an additive decomposition of the elastic strain tensor into its tensile and its compression states according to

$$\boldsymbol{\varepsilon}^e = \boldsymbol{\varepsilon}_+^e + \boldsymbol{\varepsilon}_-^e, \quad \boldsymbol{\varepsilon}_+^e = \sum_{i=1}^3 \mathcal{H}(\varepsilon_i^e) \mathbf{m}_i. \quad (7)$$

Here,  $\varepsilon_i^e$  are the eigenvalues,  $\mathbf{m}_i$  are the eigenprojections of the elastic strain tensor and  $\mathcal{H}$  is the Heaviside function. Within the numerical implementation, the discontinuous Heaviside function has been approximated in line with [11] by setting numerical parameters  $g_0 = 0$ ,  $x_0 = 0$  and  $x_R = 10^{-6}$ . A straightforward calculation of the thermodynamic driving forces leads to

$$\boldsymbol{\sigma} = \frac{\partial \psi}{\partial \boldsymbol{\varepsilon}} = \lambda [\mathbf{b} : \boldsymbol{\varepsilon}_+^e + \mathbf{I} : \boldsymbol{\varepsilon}_-^e] \left[ \mathbf{b} : \frac{\partial \boldsymbol{\varepsilon}_+^e}{\partial \boldsymbol{\varepsilon}^e} + \mathbf{I} : \frac{\partial \boldsymbol{\varepsilon}_-^e}{\partial \boldsymbol{\varepsilon}^e} \right] + 2\mu \left[ [\mathbf{b} \cdot \boldsymbol{\varepsilon}_+^e \cdot \mathbf{b}] : \frac{\partial \boldsymbol{\varepsilon}_+^e}{\partial \boldsymbol{\varepsilon}^e} + \boldsymbol{\varepsilon}_-^e : \frac{\partial \boldsymbol{\varepsilon}_-^e}{\partial \boldsymbol{\varepsilon}^e} \right], \quad (8)$$

$$\boldsymbol{\alpha} = -\frac{\partial \psi}{\partial \mathbf{a}} = -H_a \mathbf{b} \cdot \mathbf{a} \cdot \mathbf{b}, \quad (9)$$

$$\boldsymbol{\kappa} = -\frac{\partial \psi}{\partial \mathbf{k}} = -H_k [\mathbf{b} : \mathbf{k}] \mathbf{b}, \quad (10)$$

$$\boldsymbol{\beta}^e = -\frac{\partial \psi^e}{\partial \boldsymbol{\varepsilon}^e} = -\lambda [\mathbf{b} : \boldsymbol{\varepsilon}_+^e + \mathbf{I} : \boldsymbol{\varepsilon}_-^e] \boldsymbol{\varepsilon}_+^e - 2\mu \boldsymbol{\varepsilon}_+^e \cdot \mathbf{b} \cdot \boldsymbol{\varepsilon}_+^e, \quad (11)$$

$$\boldsymbol{\beta}^p = -\frac{\partial \psi^p}{\partial \boldsymbol{\varepsilon}^p} = -H_a \mathbf{a} \cdot \boldsymbol{\varepsilon}^p \cdot \mathbf{a} - H_k [\mathbf{b} : \mathbf{k}] \mathbf{k}, \quad (12)$$

$$\boldsymbol{\beta} = \boldsymbol{\beta}^e + \boldsymbol{\beta}^p, \quad (13)$$

where  $\boldsymbol{\sigma}$  is the stress tensor,  $\boldsymbol{\alpha}$  is the back stress tensor,  $\boldsymbol{\kappa}$  is the drag stress tensor and  $\boldsymbol{\beta}$  the energy release rate. Using the thermodynamic driving forces, the dissipation inequality reads in its reduced form

$$\mathcal{D}^{\text{red}} = \boldsymbol{\sigma} : \dot{\boldsymbol{\varepsilon}} - \dot{\psi} = \boldsymbol{\sigma} : \dot{\boldsymbol{\varepsilon}}^{\text{p}} + \boldsymbol{\alpha} : \dot{\boldsymbol{a}} + \boldsymbol{\kappa} : \dot{\boldsymbol{k}} + \boldsymbol{\beta} : \dot{\boldsymbol{b}} \geq 0. \quad (14)$$

By following the principle of Generalized Standard Materials [21], a plastic potential is introduced for the definition of the evolution equations. The dissipation inequality is known to be automatically fulfilled if that potential is convex, non-negative and contains the origin. That potential is specified as

$$g = \Phi(\boldsymbol{\sigma}, \boldsymbol{\alpha}, \boldsymbol{\kappa}, \boldsymbol{b}) + \Gamma_{\alpha}(\boldsymbol{\alpha}, \boldsymbol{b}) + \Gamma_{\beta}(\boldsymbol{\beta}^{\text{e}}, \boldsymbol{b}) \quad (15)$$

and consists of the yield function  $\Phi$  and non-associated parts  $\Gamma_{\alpha}$  and  $\Gamma_{\beta}$ . The yield function is chosen as

$$\Phi = \sqrt{\bar{\tau}} - \tau_y - \frac{1}{3} \boldsymbol{b}^{-1} : \boldsymbol{\kappa} - \Delta\tau \left[ 1 - \exp\left(-\frac{|\boldsymbol{b}^{-1} : \boldsymbol{\kappa}|}{\kappa_{\text{u}}}\right) \right], \quad (16)$$

$$\bar{\tau} = \frac{3}{2} \boldsymbol{b}^{-1} : [\boldsymbol{\tau} \cdot \boldsymbol{b}^{-1} \cdot \boldsymbol{\tau}] - \frac{1}{2} [\boldsymbol{b}^{-1} : \boldsymbol{\tau}]^2 \quad \text{with } \boldsymbol{\tau} = \boldsymbol{\sigma} - \boldsymbol{\alpha}, \quad (17)$$

where the equivalent stress  $\sqrt{\bar{\tau}}$  is of von Mises-type and depends on the relative stress tensor  $\boldsymbol{\tau}$ . According to Eq. (16), the yield function captures linear and exponential isotropic hardening. The respective model parameters are denoted as  $\tau_y$ ,  $\Delta\tau$  and  $\kappa_{\text{u}}$ . The non-associative parts of potential (15) are given as

$$\Gamma_{\alpha} = \frac{B_{\text{a}}}{2H_{\text{a}}} \boldsymbol{b}^{-1} : [\boldsymbol{\alpha} \cdot \boldsymbol{b}^{-1} \cdot \boldsymbol{\alpha}], \quad (18)$$

$$\Gamma_{\beta} = \frac{\eta_1}{2} [\boldsymbol{b}^m : \boldsymbol{\beta}^{\text{e}}]^2 + \frac{\eta_2}{2} \boldsymbol{b}^m : [\boldsymbol{\beta}^{\text{e}} \cdot \boldsymbol{b}^m \cdot \boldsymbol{\beta}^{\text{e}}] \quad (19)$$

and extend the model to non-linear kinematic hardening of Armstrong-Frederick type with model parameter  $B_{\text{a}}$ , cf. [22]. The damage evolution is controlled by potential  $\Gamma_{\beta}$  and consists of an isotropic part (damage modulus  $\eta_1$ ) and an anisotropic part (damage modulus  $\eta_2$ ). The damage exponent  $m$  allows for greater flexibility when calibrating the model to experiments. Furthermore, potential  $\Gamma_{\beta}$  depends only on the elastic part of the energy release rate  $\boldsymbol{\beta}$ . This novel modification of the original model ensures that no damage evolution occurs under compression. The evolution equations follow as gradients of plastic potential (15) – in line with the principle of Generalized Standard Materials – and read

$$\dot{\boldsymbol{\varepsilon}}^{\text{p}} = \dot{\lambda} \frac{\partial g}{\partial \boldsymbol{\sigma}}, \quad \dot{\boldsymbol{a}} = \dot{\lambda} \frac{\partial g}{\partial \boldsymbol{\alpha}}, \quad \dot{\boldsymbol{k}} = \dot{\lambda} \frac{\partial g}{\partial \boldsymbol{\kappa}}, \quad \dot{\boldsymbol{b}} = \dot{\lambda} \frac{\partial g}{\partial \boldsymbol{\beta}} = \dot{\lambda} \frac{\partial g}{\partial \boldsymbol{\beta}^{\text{e}}}, \quad (20)$$

which concludes the constitutive model.

*Isotropic model.* By setting  $\eta_2 = 0$ , an isotropic damage model is obtained. This case will also be employed within the numerical experiments.

## 2.2. LEM-Model – Effective Stress Concept (Lemaitre model)

The second model is adopted from [19] and is based on the principle of strain equivalence. Gibbs energy  $\mathcal{G}$  is specified as

$$\mathcal{G} = \mathcal{G}^{\text{e}} + \boldsymbol{\sigma} : \boldsymbol{\varepsilon}^{\text{p}} - \psi^{\text{p}}, \quad (21)$$

$$\mathcal{G}^{\text{e}} = \frac{1+2\nu}{2E} [\boldsymbol{H} : [\boldsymbol{\sigma}_+^{\text{dev}} \cdot \boldsymbol{H} \cdot \boldsymbol{\sigma}_+^{\text{dev}}] + \boldsymbol{\sigma}_-^{\text{dev}} : \boldsymbol{\sigma}_-^{\text{dev}}] + \frac{1-2\nu}{2E} \left[ \frac{\langle \sigma^{\text{hyd}} \rangle^2}{1-\eta D^{\text{hyd}}} + \langle -\sigma^{\text{hyd}} \rangle^2 \right], \quad (22)$$

$$\psi^{\text{p}} = \frac{1}{2} K \boldsymbol{a} : \boldsymbol{a} + R_{\text{inf}} \left[ p + \frac{\exp(-cp)}{c} \right] \quad (23)$$

and depends on model parameters Young's modulus  $E$ , Poisson's ratio  $\nu$ , damage parameter  $\eta$ , the isotropic hardening parameters  $R_{\text{inf}}$  and  $c$ , and the kinematic hardening modulus  $K$ . The additive decomposition of the total strains into elastic and plastic parts is again considered as  $\boldsymbol{\varepsilon} = \boldsymbol{\varepsilon}^e + \boldsymbol{\varepsilon}^p$ . Furthermore, the stress tensor is decomposed into a deviatoric ( $\boldsymbol{\sigma}^{\text{dev}}$ ) and a hydrostatic part ( $\sigma^{\text{hyd}} \mathbf{I}$ ) and subsequently into their respective positive and negative parts in order to capture the MCR-effect. Strain-like variables  $\boldsymbol{\alpha}$  and  $p$  are suitable for kinematic and isotropic hardening, respectively. The damage evolution is captured by means of second-order tensor  $\mathbf{D}$ , which enters energy (22) in terms of variables

$$D^{\text{hyd}} := \frac{1}{3} \text{tr}(\mathbf{D}), \quad \mathbf{H} := [\mathbf{I} - \mathbf{D}]^{-\frac{1}{2}}.$$

While undamaged material is represented by  $\mathbf{D} = \mathbf{0}$ , at least one eigenvalue of  $\mathbf{D}$  converges to one for completely damaged material points.

The thermodynamic driving forces follow as the derivatives of  $\mathcal{G}$  and read

$$\boldsymbol{\varepsilon}^e = \frac{\partial \mathcal{G}}{\partial \boldsymbol{\sigma}} = \frac{1 + \nu}{E} [\text{dev}(\mathbf{H} \cdot \boldsymbol{\sigma}_+^{\text{dev}} \cdot \mathbf{H}) + \boldsymbol{\sigma}_-^{\text{dev}}] + \frac{1 - 2\nu}{E} \left[ \frac{\langle \sigma^{\text{hyd}} \rangle}{1 - \eta D^{\text{hyd}}} - \langle -\sigma^{\text{hyd}} \rangle \right] \mathbf{I}, \quad (24)$$

$$\boldsymbol{\alpha} = -\frac{\partial \mathcal{G}}{\partial \boldsymbol{\alpha}} = \frac{2}{3} K \boldsymbol{\alpha}, \quad (25)$$

$$q = -\frac{\partial \mathcal{G}}{\partial p} = R_{\text{inf}} [1 - \exp(-cp)], \quad (26)$$

$$\mathbf{Y} = -\frac{\partial \mathcal{G}}{\partial \mathbf{D}} = -\frac{1 + 2\nu}{E} [\boldsymbol{\sigma}_+^{\text{dev}} \cdot \mathbf{H} \cdot \boldsymbol{\sigma}_+^{\text{dev}}] : \frac{\partial \mathbf{H}}{\partial \mathbf{D}} - \eta \frac{1 - 2\nu}{6E} \frac{\langle \sigma^{\text{hyd}} \rangle^2}{[1 - \eta D^{\text{hyd}}]^2} \mathbf{I}. \quad (27)$$

The transformation of Gibbs energy  $\mathcal{G}$  into Helmholtz energy  $\psi$  reads

$$\psi = \boldsymbol{\sigma} : \boldsymbol{\varepsilon} - \mathcal{G} = \boldsymbol{\sigma} : \boldsymbol{\varepsilon} - \mathcal{G}^e - \boldsymbol{\sigma} : \boldsymbol{\varepsilon}^p + \psi^p \quad (28)$$

and allows to derive the reduced dissipation inequality as

$$\mathcal{D}^{\text{red}} = \boldsymbol{\sigma} : \dot{\boldsymbol{\varepsilon}} - \dot{\psi} = \boldsymbol{\sigma} : \dot{\boldsymbol{\varepsilon}}^p - \mathbf{Y} : \dot{\mathbf{D}} - \boldsymbol{\alpha} : \dot{\boldsymbol{\alpha}} - q \dot{p} \geq 0. \quad (29)$$

Following the principle of Generalized Standard Materials once again, plastic potential  $g$  is specified. Analogously to the previous model,  $g$  is assumed to be of type

$$g = \Phi(\boldsymbol{\sigma}, \boldsymbol{\alpha}, \mathbf{D}, q) + \Gamma_\alpha(\boldsymbol{\alpha}) \quad (30)$$

with von Mises-type yield function

$$\Phi = \sqrt{\bar{\tau}} - \tau_y - q \quad \text{with } \bar{\tau} = \frac{3}{2} \boldsymbol{\tau} : \boldsymbol{\tau}, \quad \boldsymbol{\tau} = \mathbf{H} \cdot \boldsymbol{\sigma}^{\text{dev}} \cdot \mathbf{H} - \boldsymbol{\alpha} \quad (31)$$

and initial yield limit  $\tau_y$ . The non-associative part of potential (30) extends the model to non-linear kinematic hardening and reads

$$\Gamma_\alpha = \frac{3\gamma}{4K} \boldsymbol{\alpha} : \boldsymbol{\alpha} \quad (32)$$

with the non-linear kinematic hardening parameter  $\gamma$ . The evolution equations then result in

$$\dot{\boldsymbol{\varepsilon}}^p = \dot{\lambda} \frac{\partial g}{\partial \boldsymbol{\sigma}}, \quad \dot{\boldsymbol{\alpha}} = -\dot{\lambda} \frac{\partial g}{\partial \boldsymbol{\alpha}}, \quad \dot{p} = -\dot{\lambda} \frac{\partial g}{\partial q} = \dot{\lambda}. \quad (33)$$

The evolution equation for damage tensor  $\mathbf{D}$  is adopted from an isotropic potential-based formulation by assuming that the rate of the damage tensor is given by the rate of the plastic strains, cf. [19]. To be more

specific,

$$\dot{\mathbf{D}} = [P\bar{Y}]^s |\dot{\varepsilon}^P|, \quad (34)$$

$$\text{with } \bar{Y} = \frac{1+\nu}{2E} \text{tr} \left( [\mathbf{H} \cdot \boldsymbol{\sigma}_+^{\text{dev}} \cdot \mathbf{H}]^2 \right) + \frac{3-6\nu}{2E} \eta \frac{\langle \sigma^{\text{hyd}} \rangle^2}{[1-\eta D^{\text{hyd}}]^2} \quad (35)$$

with model parameters  $P$  and  $s$ . Moreover, the evolution is formulated by means of a scalar-valued energy release rate  $\bar{Y}$ , where norm  $|\bullet|$  applies the absolute value to each component of the tensor.

*Isotropic model.* The isotropic version of this model results through the modification of eq. (34) into its spherical counterpart. Here, the choice

$$\dot{\mathbf{D}} = [\hat{P}\bar{Y}]^{\hat{s}} \varepsilon^{\text{p,eq}} \mathbf{I} \quad (36)$$

is made by utilizing Eq. (3). This choice has been made since it leads to similar results as the underlying anisotropic model when considering a uniaxial tensile test.

### 2.3. Model calibration

All four models the isotropic and the anisotropic ECC model (ECC-i and ECC-a) as well as the isotropic and the anisotropic LEM model (LEM-i and LEM-a) are calibrated to experimental data from [23] for comparability and a link to applications in forming technology. The tensile test of case-hardened steel 16MnCrS5 up to strain amplitudes of  $\varepsilon_{11} \approx 0.13$  forms the basis. For this range of deformation, the strains are spatially homogeneous and necking does not occur. Both models, the anisotropic ECC model (ECC-a) and the anisotropic LEM model (LEM-a) were calibrated by means of a standard least-squares approach, while elastic parameters  $\lambda$  and  $\mu$  and the initial yield stress  $\tau_y$  were calculated beforehand. Subsequently, the isotropic models (ECC-i and LEM-i) were considered where for the sake of comparison only the damage-related parameters were recalibrated. A visualization of the calibrations is shown in Fig. 1 and the final list of model parameters is given in Tab. 1 and 2.

Parameter name	Symbol	Value	Unit
First Lamé parameter	$\lambda$	118870	MPa
Second Lamé parameter	$\mu$	79249	MPa
Yield stress	$\tau_y$	308.260	MPa
Kinematic hardening modulus	$\hat{H}_a$	7728.863	MPa
Armstrong-Frederick extension	$B_a$	38.218	-
Isotropic hardening modulus	$H_k$	$1.829 \cdot 10^{-4}$	MPa
Isotropic hardening increment	$\Delta\tau_y$	$2.261 \cdot 10^{-2}$	MPa
Isotropic hardening parameter	$\kappa_u$	0.159	MPa
Anisotropic (ECC-a model)			
Isotropic damage modulus	$\eta_1$	0.0	MPa <sup>-1</sup>
Anisotropic damage modulus	$\eta_2$	14.503	MPa <sup>-1</sup>
Damage exponent	$m$	11.217	-
Isotropic (ECC-i model)			
Isotropic damage modulus	$\hat{\eta}_1$	14.408	MPa <sup>-1</sup>
Anisotropic damage modulus	$\hat{\eta}_2$	0.0	MPa <sup>-1</sup>
Damage exponential	$\hat{m}$	11.373	-

Table 1: Model parameters of the ECC model. Parameters associated with the isotropic damage model are indicated with a superposed hat  $\hat{\bullet}$ .

Both models match the experimental data well, see Figure 1 (a). The largest error between the experiments and the calibration is associated with the LEM-a model and occurs at a strain of  $\varepsilon_{11} = 0.07$ . However, the respective error is below 10 MPa and hence, less than 2.5%. The behavior with respect to a shear mode is additionally shown in Figure 1 (c) in order to highlight the models' different response – the shear mode

Parameter name	Symbol	Value	Unit
First Lamé parameter	$\lambda$	118875.0	MPa
Second Lamé parameter	$\mu$	79250.0	MPa
Yield stress	$\tau_y$	308.26	MPa
Isotropic hardening parameter	$\hat{c}$	0.1854	-
Kinematic hardening modulus	$K$	42155.7	MPa
Nonlinear kinematic parameter	$\gamma$	7133.5	MPa <sup>-1</sup>
Saturation hardening stress	$R_{\text{inf}}$	26452.0	MPa
Anisotropic (LEM-a model)			
Damage parameter	$\eta$	1.0	-
Damage scale	$P$	1256.7	MPa <sup>-1</sup>
Damage exponent	$s$	0.2	-
Isotropic (LEM-i model)			
Damage parameter	$\hat{\eta}$	1.0	-
Damage scale	$\hat{P}$	623.1	MPa <sup>-1</sup>
Damage exponent	$\hat{s}$	0.2	-

Table 2: Model parameters of the LEM model. Parameters associated with the isotropic damage model are indicated with a superposed hat  $\hat{\bullet}$ .

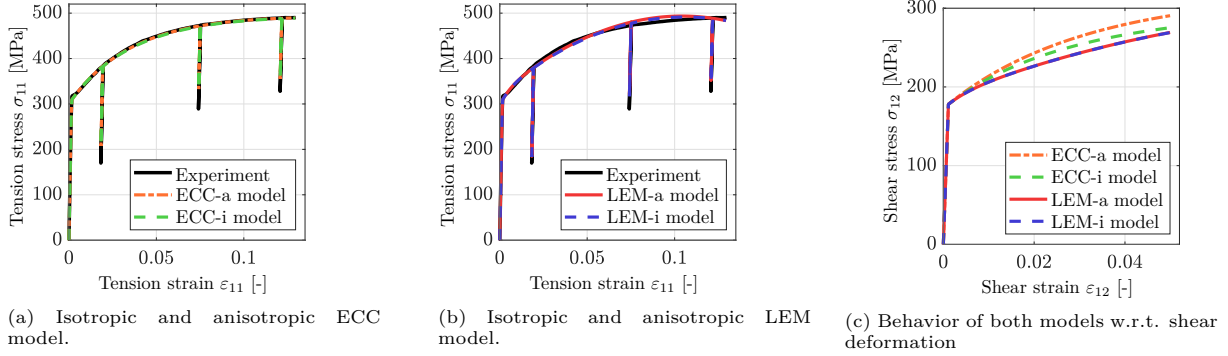


Figure 1: Experiment vs. simulation: Uniaxial tensile test with sequential unloading and numerical shear test

was not part of the calibration. Both models show qualitatively similar behavior with a maximum deviation of less than 8%. It shall be underlined that different models are used for a better and model-independent interpretation of the results. An evaluation of the individual models themselves is not intended and clearly depends on the intended application.

**Remark 1.** *The constitutive models are evaluated at the material point level due to the spatially constant stress and strain field (no necking). Therefore, no regularization is required. If boundary value problems with localization are to be analyzed, a micromorphic regularization in order to render finite element simulations well-posed is included in the models. The respective energy contributions are, however, disregarded in this work, cf. [24, 25].*

### 3. Methodology of evaluation: load path parametrization and damage measures

The analysis of various load paths is a key of the present evaluation of damage descriptions. For that reason, the parametrization of the load paths is explained in the following Subsection 3.1. As one example of the various enforced stress and/or strain paths, the predictions of the previously introduced models will be compared along identical stress triaxialities and/or Lode angle parameters. Characteristic damage measures are furthermore defined in Subsection 3.2 and based on elastic stiffness and elastic compliance tensors. Each of these measures allows to evaluate specific types of material degradation. For example, the Frobenius norm of the elasticity tensor can be interpreted as an average elasticity measure. These characteristic measures

will take the role of target functions for the load path analysis. They allow the comparison of load paths with respect to their damage impact, the identification of sensitivities and the exploration of missing influences.

### 3.1. Parametrization of load paths

The numerical studies that follow in the next section analyze the behavior of a representative material point. The mechanical loading of these points will hence be defined by prescribing either components of the stress or the strain tensor. Since these tensors are energetically dual, symmetric second-order tensors, one has to prescribe precisely six components in total. The dual six components follow as reactions. For instance, a strain-driven uniaxial tensile test corresponds to the following strain and stress tensors — boxed components are prescribed, the other ones follow as reactions:

$$\boldsymbol{\varepsilon} = \begin{bmatrix} \boxed{\varepsilon_{11}} & \varepsilon_{12} & \varepsilon_{13} \\ \text{sym} & \varepsilon_{22} & \varepsilon_{23} \\ \text{sym} & \text{sym} & \varepsilon_{33} \end{bmatrix}_{[e_1, e_2, e_3]} \quad \boldsymbol{\sigma} = \begin{bmatrix} \sigma_{11} & \boxed{\sigma_{12}} & \boxed{\sigma_{13}} \\ \text{sym} & \boxed{\sigma_{22}} & \boxed{\sigma_{23}} \\ \text{sym} & \text{sym} & \boxed{\sigma_{33}} \end{bmatrix}_{[e_1, e_2, e_3]} \quad (37)$$

In Eq. (37), the components are defined with respect to a chosen basis  $\mathbf{e}_i$  (here, a cartesian setting is adopted). Loading is implemented by enforcing a strain in 11-direction for this example of a uniaxial tensile test. Hence, the respective components of the stress tensor are unknown, but follow from the constitutive model. The other components of the stress tensor have to vanish, prescribing  $\sigma_{ij} = 0$  except for  $\sigma_{11}$ . The evolution of prescribed components is either parametrized and discretized by piecewise linear functions of the form

$$L_{\text{pwl}}(t; \mathbf{P}) = P_i + \frac{P_i - P_j}{t_i - t_j} t \quad \text{if } t \in [t_i, t_j] \quad (38)$$

or by Bézier curves defined as

$$L_{\text{Bez}}(t; \mathbf{Q}) = \sum_{i=0}^N \binom{N}{i} [1-t]^{N-i} t^i Q_i \quad (39)$$

with control points  $P_i$  and  $Q_i$ , respectively. The time is normalized within the interval  $t \in [0; 1]$ , where the time-scaling is irrelevant since rate-independent models are considered.

From the perspective of the numerical implementation, prescribing components of the stress tensor requires an iteration. This is implemented by a constitutive driver where the respective constraints are solved by means of a Newton-iteration. An analogous procedure is also employed for controlling the stress triaxiality and/or the Lode (angle) parameter.

### 3.2. Characteristic damage measures and target functions

Characteristic damage measurements are defined in order to compare the damage evolution along the load paths and between different models. Since the internal variables capturing damage are not identical for both basic models, the respective elastic stiffness and elastic compliance tensors are instead considered for the definition of suitable damage measures. Elastic stiffness tensor and elastic compliance tensors are inverse to each other, i.e.,  $\mathbb{E}^e : \mathbb{C}^e = \mathbb{I}$  with  $\mathbb{I}$  being the symmetric fourth-order identity. Starting from the Helmholtz energy  $\psi$ , the elastic moduli of the ECC-model are obtained as

$$[\mathbb{E}_{\text{ECC}}^e]_{ijkl} := \frac{\partial^2 \psi}{\partial \varepsilon_{ij} \partial \varepsilon_{kl}} = \lambda [b_{ij} b_{kl}] + \mu [b_{ik} b_{jl} + b_{il} b_{jk}]. \quad (40)$$

Likewise, the LEM-model yields the elastic compliance

$$[\mathbb{C}_{\text{LEM}}^e]_{ijkl} := \frac{\partial^2 \mathcal{G}}{\partial \sigma_{ij} \partial \sigma_{kl}} = \frac{1+\nu}{E} \left[ \frac{1}{2} [H_{ik} H_{jl} + H_{il} H_{jk}] - \frac{1}{3} [\delta_{ij} H_{km} H_{ml} + H_{in} H_{nj} \delta_{kl}] \right. \\ \left. + \frac{1}{9} \left[ H_{op} H_{op} + \frac{3}{1-\eta D^{\text{hyd}}} \right] \delta_{ij} \delta_{kl} \right] - \frac{\nu}{E} \frac{1}{1-\eta D^{\text{hyd}}} \delta_{ij} \delta_{kl} \quad (41)$$



where  $\delta_{ij}$  is the Kronecker-Delta.

Effective-scalar-valued variables can be introduced based on either the elastic stiffness or the elastic compliance tensor. For instance, the Frobenius-norm of the fourth-order elasticity tensor

$$f_{\mathbb{E}} := \sqrt{\mathbb{E}^e :: \mathbb{E}^e} \quad (42)$$

with  $::$  denoting a quadruple contraction, defines a suitable average value of  $\mathbb{E}^e$ . Based on Eq. (42) and denoting the elasticity tensor associated with a reference model or load path as  $\bar{\mathbb{E}}$ , the difference between two load paths (or model descriptions) can be defined as

$$f_{\mathbb{E}}^{\text{diff}} = \left[ \sqrt{\mathbb{E}^e :: \mathbb{E}^e} - \sqrt{\bar{\mathbb{E}} :: \bar{\mathbb{E}}} \right]^2. \quad (43)$$

Often, the undamaged configuration represents a natural reference solution, i.e.,  $\bar{\mathbb{E}}^e = \mathbb{E}^e(t=0)$ . As an alternative to the Frobenius-norm (42), the directional elastic stiffness and compliance

$$E_{\mathbf{r}} = [\mathbf{r} \otimes \mathbf{r}] : \mathbb{E}^e : [\mathbf{r} \otimes \mathbf{r}] \quad (44)$$

$$C_{\mathbf{r}} = [\mathbf{r} \otimes \mathbf{r}] : \mathbb{C}^e : [\mathbf{r} \otimes \mathbf{r}] \quad (45)$$

can be considered respectively, where unit vector  $\mathbf{r}$  defines the direction. A suitable measure for the damage accumulation based on Eq. (44) reads, for instance,

$$\xi_{\mathbb{E}} = \frac{\min_{\mathbf{r}} E_{\mathbf{r}}(\mathbf{r})}{E_0}. \quad (46)$$

Here,  $E_0$  corresponds to the initial state at  $t=0$ , which is isotropic and independent of  $\mathbf{r}$ . In contrast to measure (43), measure (46) chooses the directional-dependent lowest elasticity and thus largest damage-induced degradation. Finally, if the direction-dependent elastic modulus is to be evaluated, inverted  $C_{\mathbf{r}}$  can be compared to the reference resulting in

$$\zeta(\mathbf{r}) = \frac{C_0}{C_{\mathbf{r}}}. \quad (47)$$

#### 4. Numerical examples

This section highlights the application limits of isotropic damage representations by means of illustrative examples. As mathematical models are a compromise between accuracy and practicability, the parameters used for the prediction of damage must be chosen according to their influence and the problem of interest. Also the guidelines for forming or operational processes must relate to practical and measurable principles. Possible limitations of restricted parameter sets are thus accompanied by load paths where differences can be observed. First, the well-known statement

- The smaller the stress triaxiality, the smaller the damage accumulation (see [26] and Subsection 4.1)

as well as

- Damage accumulation is uniquely governed by the stress triaxiality and the Lode (angle) parameter (see [27])

are analyzed. It is shown that load paths can indeed be designed by means of optimization algorithms that contradict both statements. Second, the concept of a fracture surface in line with [12, 13] is investigated in Subsection 4.2. This concept is based on the statement

- Damage accumulation is uniquely governed by the triple stress triaxiality, Lode (angle) parameter and equivalent plastic strain (see [27] and Subsection 4.2).

Optimization algorithms again show that this statement does also not hold true in general – particularly for complex load paths. Since the present studies rely on numerical experiments, i.e., constitutive modeling, two different models with isotropic and anisotropic variants are considered. The respective parameters are given in Table 1 and Table 2.

#### 4.1. The smaller the stress triaxiality, the smaller the damage accumulation? Coupled tension-torsion experiments

Inspired by combined axial/torsional test systems and with the goal of multi-directional load paths in mind, the tension-torsion problem sketched in Figure 2 is considered for a cylindrical coordinate system  $[\mathbf{e}_r, \mathbf{e}_\theta, \mathbf{e}_z]$ . A virtual sequential tension-torsion test serves as the reference load path. Within this test,  $\varepsilon_{\theta z}$  is increased

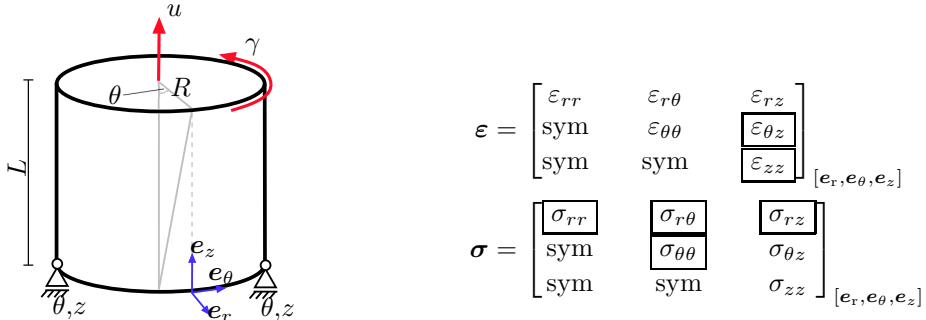


Figure 2: Combined axial/torsional test: sketch of mechanical system and boundary conditions in terms of prescribed stress and strains. Prescribed coordinates are boxed. According to the underlying kinematics,  $\varepsilon_{zz} = u/L$  and  $\varepsilon_{\theta z} = 1/2 \gamma R/L$ .

first up to an amplitude of  $\varepsilon_{\theta z} = 0.03$ , while enforcing  $\varepsilon_{zz} = 0$ . Subsequently,  $\varepsilon_{zz}$  is increased up to  $\varepsilon_{zz} = 0.06$ . During this second loading stage,  $\varepsilon_{\theta z} = 0.03$  is kept constant. The final strain components at normalized time  $t = 1$  are  $\varepsilon_{zz} = 0.06$  and  $\varepsilon_{\theta z} = 0.03$ . The evolution of the stress-triaxiality corresponding to this reference load path is denoted by  $\eta^{\text{ref}}(t)$  and the Frobenius-norm of the final elastic stiffness tensor is  $f_{\mathbb{E}}^{\text{ref}}(t = 1)$ . Since four different models are analyzed, four different reference solutions are computed (isotropic and anisotropic ECC-model, isotropic and anisotropic LEM-model).

Next, load path variations are parametrized to search for damage-mitigating alternatives with higher stress triaxialities. These would then provide counter examples for the first statement (“The smaller the stress triaxiality, the smaller the damage accumulation”). Strain components  $\varepsilon_{\theta z}$  and  $\varepsilon_{zz}$  are discretized by means of fifth-order Bézier curves, see Eq. (39). While the initial conditions are  $\varepsilon_{\theta z}(t = 0) = \varepsilon_{zz}(t = 0) = 0$ , the final state is defined by  $\varepsilon_{\theta z}(t = 1) = 0.03$  and  $\varepsilon_{zz}(t = 1) = 0.06$ . The other coordinates of the Bézier representation are computed by mitigating the final damage state in the sense of an optimization. To be more precise, the following optimization problem is considered:

Optimal damage path: (48)

Maximize average elastic stiffness:  $f_{\mathbb{E}}(t = 1)$

Subjected to stress triaxiality constraint:  $\eta^{\text{opt}}(t) \geq \eta^{\text{ref}}(t) \forall t \in [0, 1]$

Parameter space: Parameters  $Q_i$  of Bézier representation of the load paths

Accordingly, the load path which maximizes the average elastic stiffness is sought for. This path has to fulfill the constraint  $\eta^{\text{opt}}(t) \geq \eta^{\text{ref}}(t) \forall t$ . As a consequence, optimal load paths that contradict the statement “the smaller the stress triaxiality, the smaller the damage accumulation” are to be identified. Since the resulting optimization problem is highly non-convex, a two-stage gradient-free optimization method is employed. To

be more explicit, a particle swarm optimization (see [28]), followed up by a Nelder-Mead simplex algorithm (see [29]) is employed. The inequality corresponding to the stress triaxiality ( $\eta^{\text{opt}}(t) \geq \eta^{\text{ref}}(t) \forall t$ ) is enforced by means of a penalty function.

The results in Figure 3 correspond to eight different simulations – four constitutive models (isotropic and anisotropic ECC-model, isotropic and anisotropic LEM-model) times two load paths (reference path and optimized path). It can be seen that the optimized paths indeed lead to less damage, i.e., the average

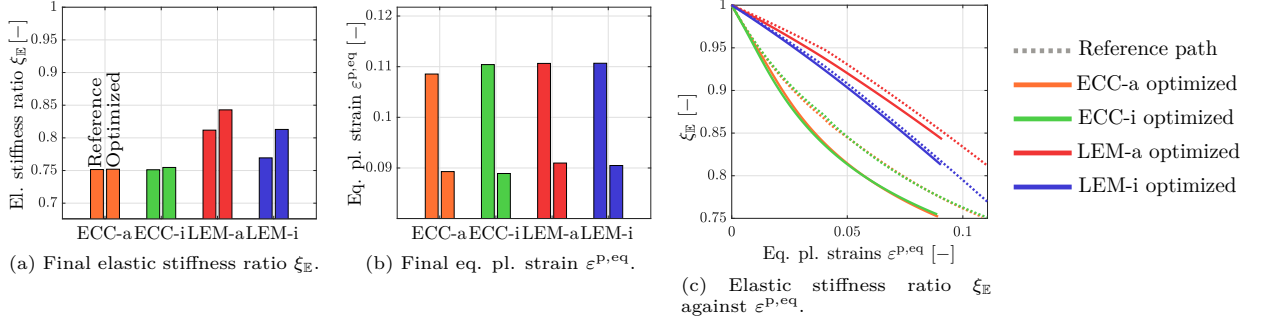


Figure 3: Combined axial/torsional test: (a) Final elastic stiffness ratio  $\xi_{\mathbb{E}}(t = 1)$  and (b) final equivalent plastic deformation  $\varepsilon^{\text{P,eq}}(t = 1)$  for all four constitutive models and for the reference load path (left bars) as well as for the optimized load path (right bars). (c) Evolution of effective stiffness ratio  $\xi_{\mathbb{E}}$  in terms of  $\varepsilon^{\text{P,eq}}$ .

elastic stiffness is larger for such paths, see the right columns in diagram 3 (a). Since ductile damage is primarily driven by plastic deformations, one might expect that  $\varepsilon^{\text{P,eq}}$  is smaller for the optimized paths. This is confirmed in diagram 3 (b). For this reason, a low equivalent plastic strain is suggested as a further damage-mitigating indicator. This hypothesis can also be drawn from diagram 3 (c). Instead of showing the evolution of effective measure  $f_{\mathbb{E}}$  in terms of the (pseudo) time, a parametrization in terms of the equivalent plastic strain is used. As evident a smaller value of  $f_{\mathbb{E}}$  is accompanied by a larger value of  $\varepsilon^{\text{P,eq}}$ . The influence of  $\varepsilon^{\text{P,eq}}$  will be examined in the next subsection.

According to Figure 4 (b), the stress triaxiality of the optimized paths is always higher than that of the reference paths, i.e., inequality  $\eta^{\text{opt}}(t) \geq \eta^{\text{ref}}(t)$  is indeed fulfilled at any time. As evident from Figure 4 (a),

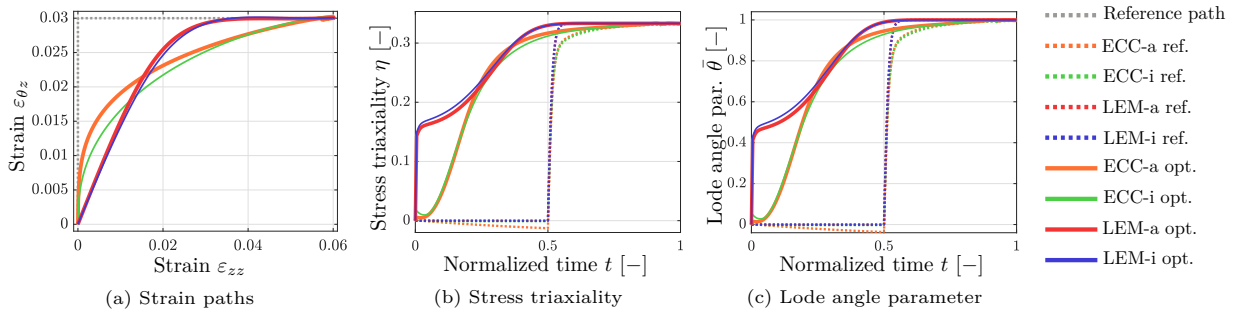


Figure 4: Combined axial/torsional test: Reference and optimized load paths for different ductile damage models. Reference paths are represented by dotted lines, optimized load paths by solid lines.

shear component  $\varepsilon_{\theta z}$  and axial component  $\varepsilon_{zz}$  of the strain tensor are simultaneously applied for the optimal paths – in contrast to the sequential reference path. Finally, the evolution of the Lode angle parameter is shown in Figure 4 (c). The evolution is similar to that of the stress triaxiality. In particular, the Lode angle parameter of the optimal path is always larger than its referential counterpart.

A more detailed comparison of the material degradation at the final time  $t = 1$  is given in Figure 5. It shows the directional elastic stiffness ratio of the anisotropic damage models ECC-a and LEM-a relative to the initial isotropic, undamaged state. While the model LEM-a leads to an almost isotropic material degradation,

the model ECC-a predicts a more pronounced anisotropy. For both constitutive models, nevertheless, the optimized load paths are characterized by a larger elastic stiffness compared to the reference solution. Stress triaxiality – even in combination with the equivalent plastic strain – hence remain an insufficient indicator for damage alone and independent of the models.

#### 4.2. Is damage accumulation uniquely governed by the triple stress triaxiality, Lode (angle) parameter and equivalent plastic strain?

It has been shown in the previous section that the stress triaxiality as well as the equivalent plastic strain are primary influencing factors of ductile damage. However, it has also been shown that these factors are not sufficient in order to characterize anisotropic material degradation under complex load paths. For this reason, the Lode angle parameter is often also considered. A frequently employed continuum damage mechanics framework based on the stress triaxiality, the Lode angle parameter as well as the equivalent plastic strain and relates to so-called *fracture surfaces*, cf. [12, 13]. Within these models, the damage evolution is proportional to the plastic strain rate and a scaling factor. The latter is a function in terms of the triple stress triaxiality, Lode angle parameter and the equivalent plastic strain. It will be shown in this section that even this ansatz is still not sufficient for a full characterization of ductile damage accumulation. Fracture surfaces, such as those in [12, 13], can be interpreted as iso-surfaces of an equivalent scalar-valued damage measure. Accordingly, they can be computed for a certain model by connecting triples of stress triaxiality, Lode angle parameter and the equivalent plastic strain to the same equivalent damage measure. First, such surfaces are computed in paragraph 4.2.1 for proportional load paths. Subsequently, the influence of more complex load paths is studied in paragraph 4.2.2 as well as in paragraph 4.2.3.

##### 4.2.1. Fracture surfaces for proportional loading

In order to compute iso-surfaces of damage, a suitable scalar-valued measure is required. In this section, relative directional-elastic stiffness threshold  $\xi_E = 0.8$  is chosen for that purpose. Accordingly, the fracture surface is defined by states corresponding to a directional stiffness of 80% compared to the undamaged state. Clearly other measures and thresholds are also possible. Starting from the initial unloaded configuration, the stresses are increased until threshold  $\xi_E = 0.8$  is reached. For the whole load path, the stress triaxiality and the Lode angle parameter are kept constant (proportional loading). To be more precise, the stress tensor is prescribed as

$$\boldsymbol{\sigma} = \begin{bmatrix} \boxed{\sigma_{11}} & & & \\ \text{sym} & \boxed{0} & & \\ & \boxed{\sigma_{22}(\sigma_{11}, \eta, L)} & & \\ \text{sym} & & \boxed{0} & \\ & & \boxed{0} & \\ & & & \boxed{\sigma_{33}(\sigma_{11}, \eta, L)} \end{bmatrix}_{[e_1, e_2, e_3]} \quad (49)$$

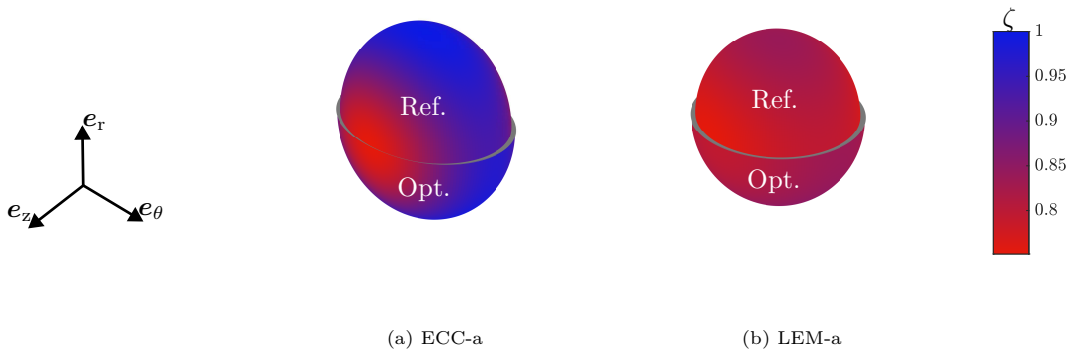


Figure 5: Combined axial/torsional test: Directional elastic stiffness ratio for anisotropic damage evolution relative to initial material. Comparison between optimized (lower) and reference paths (upper hemispheres) for  $t = 1$ .

where  $\eta$  is the (prescribed) stress triaxiality and  $L$  the (prescribed) Lode parameter. It is noted here that Eq. (2) represents a unique mapping of the Lode parameter  $L$  to the Lode angle parameter  $\bar{\theta}$ . Closed-form solutions for  $\sigma_{22}(\sigma_{11}, \eta, L)$  and  $\sigma_{33}(\sigma_{11}, \eta, L)$  are given in Appendix A. Thus, the only free loading parameter is  $\sigma_{11}$ . This parameter is increased until the damage threshold is reached.  $17 \times 13$  tuples of stress triaxiality and Lode angle parameter are considered in order to span the fracture surface. The fracture surfaces predicted by the different models are summarized in Figure 6. It shall be noted that the comparison of the models does not aim at their individual evaluation but rather at finding model-invariant conclusions on the damage evolution and the corresponding input parameters. In line with [12, 13], the ECC

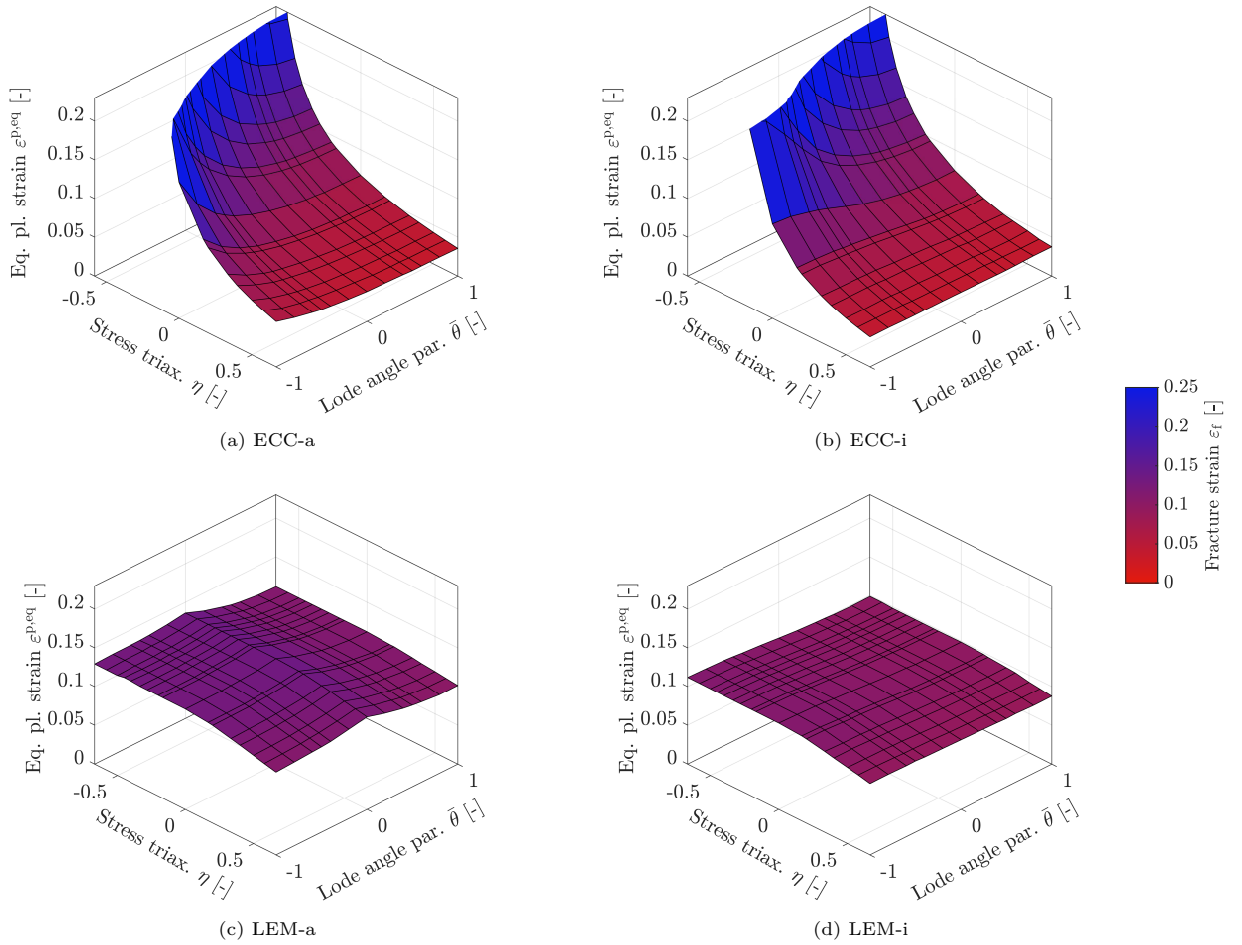


Figure 6: Fracture surfaces induced by the four different CDM-based models (ECC-a, ECC-i, LEM-a, LEM-i) for proportional load paths. The surfaces correspond to a damage isosurfaces of  $\xi_{\mathbb{E}} = 0.8$ , i.e., 80% remaining directional stiffness compared to the undamaged initial state. The surfaces have been computed by prescribing the proportional load path of uniaxial tension.

model shows the trend the smaller the stress triaxialities, the larger the equivalent plastic strains – both for the anisotropic and for the isotropic formulation. The ECC model does not predict damage evolution for biaxial compression. Although the stress triaxiality is the major influencing factor of the stress state, the fracture surface corresponding to the ECC model also depends on the Lode angle parameter with the largest sensitivity for small stress triaxialities.

In contrast to the ECC model, the fracture surface predicted by the LEM model is less sensitive with respect to the stress triaxialities and the Lode angle parameter, see Figures 6 (c) and (d). However, the overall trend is similar: The smaller the stress triaxialities, the larger the equivalent plastic strains. Only for larger

negative triaxialities a plateau can be seen – in contrast to model ECC. This plateau can be partly explained by the structure of the driving force, cf. Eq. (35). Since driving force  $\bar{Y}$  is quadratic in the stress tensor, the pre-factor scaling the damage evolution is symmetric in the stress triaxiality. Clearly, the MCR-Effect dampens this effect.

#### 4.2.2. Fracture surfaces for non-proportional load paths

This paragraph analyzes whether the fracture surface is also meaningful for other loads paths (in contrast to the proportional ones before with constant stress triaxiality and Lode angle parameter). As a representative reference path, uniaxial tension is considered, i.e.,  $\boldsymbol{\sigma} = \sigma_{11} \mathbf{e}_1 \otimes \mathbf{e}_1$ . It corresponds to a stress triaxiality of  $\eta = 1/3$  and Lode angle parameter of  $L = 1$ . Inspired by uniaxial tension, the following more general stress path is considered:

$$\boldsymbol{\sigma}(t) = \begin{array}{c} \boxed{\sigma_{11}(t)} \\ \text{sym} \\ \boxed{\sigma_{22}(\sigma_{11}(t), \eta(t))} \\ \text{sym} \end{array} \begin{array}{c} \boxed{0} \\ \boxed{0} \\ \boxed{0} \end{array} \begin{array}{c} \boxed{0} \\ \boxed{0} \\ \boxed{0} \end{array} \quad [e_1, e_2, e_3] \quad (50)$$

Clearly, by setting  $\eta = 1/3$  and  $L = 1$ , uniaxial tension is recovered. However, the stress triaxiality is prescribed by means of a Bézier interpolation in time. While it corresponds to uniaxial tension for the initial and the final state, i.e.,  $\eta(t = 0) = \eta(t = 1) = 1/3$ , it reaches its maximum deviation from this state at  $t = 0.5$  with a stress triaxiality of  $\eta(t = 0.5) = 1/3 - 7/30 = 1/10$  for the first load path and  $\eta(t = 0.5) = 1/3 + 7/30 = 17/30$  for the second load path. The Lode angle parameter is not explicitly controlled, but follows from  $\sigma_{11}$  and  $\eta$ . Finally, it is noted that the time-scaling of  $\sigma_{11}(t)$  is iteratively adapted until the state  $\sigma_{11}(t = 1)$  and  $\eta(t = 1)$  correspond to uniaxial tension and a damage threshold of  $\xi_E = 0.8$ .

The aforementioned two different load paths are shown in Figure 7 in dashed and dotted lines. They are

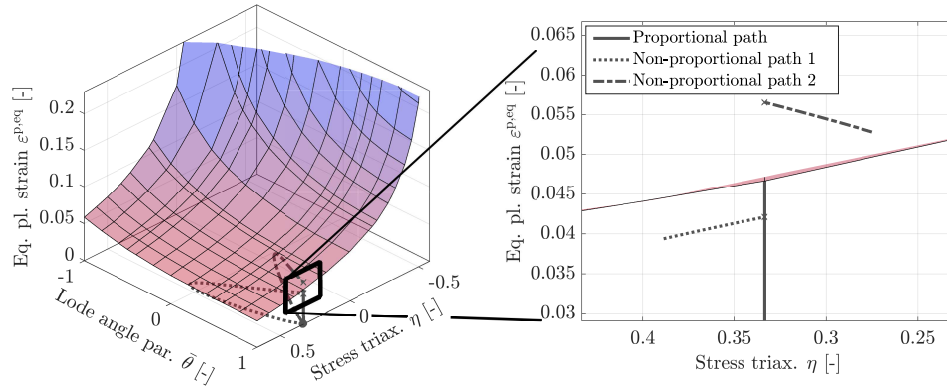


Figure 7: Fracture surface induced by CDM-based model ECC-a. The surface is a damage isosurfaces of  $\xi_E = 0.8$ , i.e., 80% remaining directional stiffness compared to the undamaged initial state. Two non-proportional load paths as defined by stress tensor (49) are also shown in green as well as in orange color. A zoom-in of a cut is shown on the right hand side. Accordingly, both nonproportional load paths are characterized by different equivalent plastic strains at final time  $t = 1$ .

represented by means of the triple equivalent plastic strain, stress triaxiality and Lode angle parameter. According to Figure 7, these paths are non-proportional in this representation and even more important, they lead to different equivalent plastic strains at the final time  $t = 1$  corresponding to  $\xi_E = 0.8$ , see the zoom-in in Figure 7 (right). The deviation of the equivalent plastic strain for these paths is above 30%. This deviation clearly confirms that a characterization and description of damage accumulation only by means of the three final influencing variables — equivalent plastic strain, stress triaxiality and Lode angle parameter

— is generally not sufficient. This holds in particular if complex, non-proportional load paths are to be analyzed.

Since the path-dependent deviation of the fracture energy also relies on the underlying constitutive model, the numerical experiment is re-computed for the other models (ECC-a, ECC-i, LEM-a, LEM-i). Again it can be seen that the triple of equivalent plastic strain, stress triaxiality and Lode angle parameter does not uniquely define a damage state, see the results summarized in Figure 8.

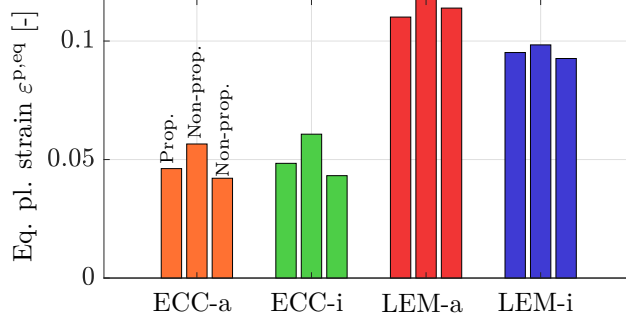


Figure 8: Accumulated equivalent plastic strain predicted by the different CDM-based models. The strain corresponds to  $\xi_E = 0.8$ , i.e., isosurface of 80% remaining directional stiffness compared to the undamaged initial state. While the red bars are associated with the proportional load path of uniaxial tension, the green as well as the orange bars correspond to the non-proportional load paths as defined by stress tensor (49)

#### 4.2.3. Non-proportional load paths with constant stress invariants

According to the previous section, a damage characterization by means of the triple equivalent plastic strain, stress triaxiality and Lode angle parameter is usually not possible for complex load paths. Since the stress triaxiality and the Lode (angle) parameter are invariants of the stress tensor (see Appendix A), one could also monitor and control all three invariants of the stress tensor (instead of just  $\eta$  and  $L$ ). This is precisely the idea analyzed in this paragraph. For that purpose, two different stress tensors are considered. While  $\boldsymbol{\sigma}$  corresponds to proportional loading,  $\tilde{\boldsymbol{\sigma}}$  is associated with a more complex load path. However, both tensors show the same evolution of their invariants (eigenvalues  $\sigma_i(t) = \tilde{\sigma}_i(t)$ ) – in particular  $\eta(t)$  and  $L(t)$  are identical for both paths. Only their directions are different (eigenvectors).  $\boldsymbol{\sigma}$  and  $\tilde{\boldsymbol{\sigma}}$  can be implemented by means of the spectral decomposition, i.e.,

$$\boldsymbol{\sigma} = \sum_{i=1}^3 \sigma_i \mathbf{N}^i \otimes \mathbf{N}^i \quad (51)$$

$$\tilde{\boldsymbol{\sigma}} = \sum_{i=1}^3 \sigma_i [\mathbf{R} \cdot \mathbf{N}^i] \otimes [\mathbf{R} \cdot \mathbf{N}^i] \quad (52)$$

$$\text{with } \mathbf{R}(\alpha, \beta, \gamma) = \mathbf{R}_{\bar{\mathbf{e}}_1}(\alpha) \cdot \mathbf{R}_{\bar{\mathbf{e}}_2}(\beta) \cdot \mathbf{R}_{\mathbf{e}_3}(\gamma) . \quad (53)$$

where  $\mathbf{N}_i$  are the eigenvectors of  $\boldsymbol{\sigma}$  and  $\mathbf{R}_{\mathbf{e}_i}$  are rotation matrices depending on the Euler angles  $\alpha$ ,  $\beta$  and  $\gamma$ . Four different mechanical tests are considered:

1. Uniaxial tension:  $\eta = 1/3$  and  $\bar{\theta} = 1$
2. Combined tension and shear:  $\eta = 1/6$  and  $\bar{\theta} = 0.506$
3. Simple shear:  $\eta = 0$  and  $\bar{\theta} = 0$
4. Combined compression and shear:  $\eta = -1/6$  and  $\bar{\theta} = -0.506$

While the first eigenvalue  $\sigma_1$  is increased, the second as well as the third follow from the prescribed and constant parameters  $\eta$  and  $L$ . To be more precise  $\sigma_2 = \sigma_2(\sigma_1, \eta, L)$  and  $\sigma_3 = \sigma_3(\sigma_1, \eta, L)$  as summarized in Appendix A are used. For the proportional load paths, stress tensor (51) with constant eigenvectors  $\mathbf{N}_i$  is considered and  $\sigma_1$  is increased up to a damage threshold of  $\xi_E = 0.8$ . In the case of the non-proportional

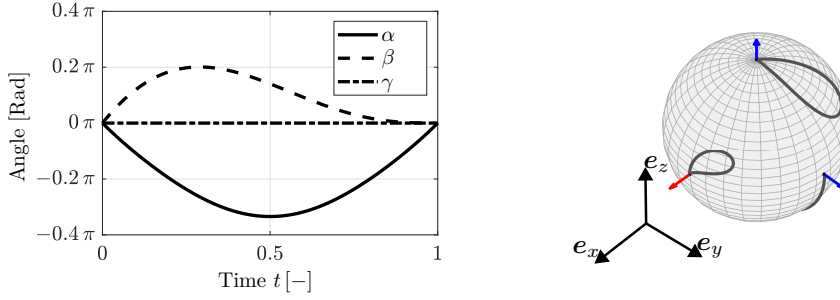


Figure 9: Euler angles  $\alpha$ ,  $\beta$  and  $\gamma$  defining a non-proportional load path according to Eqs. (52) and (53). Left: evolution of the angles in terms of normalized time  $t \in [0; 1]$ . Right: spatial rotation of the eigenvectors  $\mathbf{R} \cdot \mathbf{N}^i$ .

load paths, the evolution of the Euler angles is summarized in Figure 9. In line with the example studied in the previous paragraph, the temporal discretization of  $\sigma_1(t)$  is chosen such that all Euler angles vanish at final time  $t = 1$  as in Figure 9 when damage threshold  $\xi_{\mathbb{E}} = 0.8$  is reached, i.e., the time scaling of  $\sigma_1$  and the Euler angles is synchronized.

The results of the numerical analyses are presented in Figure 10. The bar charts summarize the results for

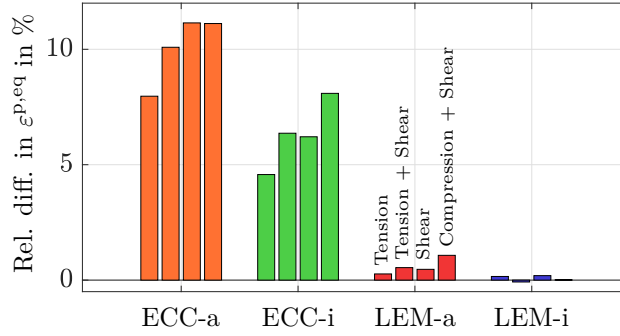


Figure 10: Relative difference of the equivalent plastic strain at final state  $\xi_{\mathbb{E}} = 0.8$  between the proportional load path (51) and the non-proportional load path (52). The bar charts summarize the results for all four models (ECC-a, ECC-i, LEM-a, LEM-i) and for all four mechanical tests (left bars: uniaxial tension; second left bars: uniaxial tension and shear; third left bars: shear; right bars: uniaxial compression and shear). For instance, the third green bar from left is associated with the ECC-i model and with shear. The relative difference of the equivalent plastic strain at final state  $\xi_{\mathbb{E}} = 0.8$  between the non-proportional and the proportional load path is slightly above 6% in this case.

all four models (ECC-a, ECC-i, LEM-a, LEM-i) and for all four mechanical tests (uniaxial tension, simple shear, combined tension and shear, combined compression and shear). It shows the relative difference of the equivalent plastic strain at final state  $\xi_{\mathbb{E}} = 0.8$  between the proportional and the non-proportional load paths. It can be seen that the anisotropic model ECC-a leads to the largest difference – followed by its isotropic counterpart ECC-i. The sensitivity on the load path is less pronounced for the models LEM. However, a minor influence is still evident – even for model LEM-i. Focusing again on the fracture surface concept, Figure 10 shows that a characterization of material damage is still not possible by considering all three invariants of the stress tensor, together with the equivalent plastic strain. Otherwise, the relative distances in Figure 10 would vanish.

The presented numerical studies showed that a characterization of ductile damage by means of only the invariants of the stress tensor is usually not sufficient. This conclusion particularly applies to a characterization of damage by means of only the stress triaxiality or the Lode (angle) parameter. While for some load paths, such isotropic approximations might lead to reasonable predictions, they are usually inadequate for complex load paths.



## 5. Conclusion

Application limits of isotropic damage characterizations for complex load paths were investigated in this paper. For that purpose, a well-established anisotropic ductile damage model (Lemaitre model) depending on the complete stress tensor was considered first and its predicted response was analyzed for different load paths. Since such numerical experiments may depend on the underlying constitutive model, a second constitutive model was additionally employed.

The first numerical experiment – inspired by a coupled tension-torsion experiment – revealed that the frequently employed recommendation ”the smaller the stress triaxiality, the smaller the damage accumulation” can be wrong for complex load paths. In order to design paths contradicting this hypothesis, an algorithm was proposed to analyze differences in the predictions and unconsidered influences.

Starting from the invariant stress triaxiality, the Lode angle parameter was additionally controlled in the next example. Since the characterization of damage by means of the stress triaxiality and the Lode angle parameter is closely related to the concept of fracture surfaces, this concept was studied in detail. In particular, fracture surfaces were computed for both ductile damage models. Again, load paths were designed showing that a damage characterization by means of the extended set of influencing variables stress triaxiality, Lode angle parameter and equivalent plastic strain is often still not possible.

Finally, the full set of invariants of the stress tensor were controlled. This can be interpreted as an isotropic approximation. However, even in this more flexible case, load paths can be designed leading to different damage accumulation.

The numerical studies showed that damage can indeed be influenced and improved by controlling the stress triaxiality as well as the Lode angle parameter. However, the remaining coordinates of the load paths still have great potential for further improvement of damage accumulation and thus, control. This potential is to be further studied, e.g., in the context of forming processes. Furthermore, the numerical studies are to be further confirmed by real experiments.

## Appendix A. Parameter realization

Denoting the eigenvalues of the stress tensor as  $\sigma_i$  with  $i = 1, 2, 3$  and  $\sigma_1 \geq \sigma_2 \geq \sigma_3$ , the stress triaxiality and the Lode parameter are defined as

$$\eta = \frac{\sqrt{2} [\sigma_1 + \sigma_2 + \sigma_3]}{3 \sqrt{[\sigma_1 - \sigma_2]^2 + [\sigma_2 - \sigma_3]^2 + [\sigma_1 - \sigma_3]^2}} \quad (\text{A.1})$$

$$L = \frac{2\sigma_2 - \sigma_1 - \sigma_3}{\sigma_1 - \sigma_3}. \quad (\text{A.2})$$

These equations can be rewritten as

$$[\sigma_2]_{1,2} = -\chi \sigma_1 \pm \sqrt{\chi^2 - \omega} |\sigma_1| \quad (\text{A.3})$$

$$[\sigma_3]_{1,2} = [a + b\chi] \sigma_1 \mp b \sqrt{\chi^2 - \omega} |\sigma_1| \quad (\text{A.4})$$

with

$$a = \frac{L+1}{L-1}, \quad b = \frac{2}{L-1}$$

and

$$\chi = \frac{18\eta^2 [L - L^2 - 2] - 4L [L - 3]}{18\eta^2 [L^2 - 3] - 2 [L - 3]^2}, \quad \omega = \frac{18\eta^2 [L^2 - L + 2] - 8L^2}{18\eta^2 [L^2 - 3] - 2 [L - 3]^2}.$$

They allow to enforce both the stress triaxiality as well as the Lode angle and to apply loading by increasing  $\sigma_1$ . Clearly, special care is required, if  $L \rightarrow 1$ .

## Acknowledgements

Financial support from the German Research Foundation (DFG) via SFB/TR TRR 188 (project number 278868966), project C01, is gratefully acknowledged. We also gratefully acknowledge the computing time provided on the Linux HPC cluster at TU Dortmund University (LiDO3), partially funded in the course of the Large-Scale Equipment Initiative by the German Research Foundation (DFG) (project number 271512359).

## References

- [1] R. I. Stephens, H. O. Fuchs (Eds.), *Metal fatigue in engineering*, 2nd Edition, A Wiley-Interscience publication, Wiley, New York Weinheim, 2001.
- [2] S. Ma, H. Yuan, Computational investigation of multi-axial damage modeling for porous sintered metals with experimental verification, *Engineering Fracture Mechanics* 149 (2015) 89–110. doi:10.1016/j.engfracmech.2015.09.049.
- [3] A. Tekkaya, P.-O. Bouchard, S. Bruschi, C. Tasan, Damage in metal forming, *CIRP Annals* 69 (2) (2020) 600–623. doi:10.1016/j.cirp.2020.05.005.
- [4] J. Koplik, A. Needleman, Void growth and coalescence in porous plastic solids, *International Journal of Solids and Structures* 24 (8) (1988) 835–853. doi:10.1016/0020-7683(88)90051-0.
- [5] A. Sancho, M. Cox, T. Cartwright, G. Aldrich-Smith, P. Hooper, C. Davies, J. Dear, Experimental techniques for ductile damage characterisation, *Procedia Structural Integrity* 2 (2016) 966–973. doi:10.1016/j.prostr.2016.06.124.
- [6] J. Lemaitre, A Continuous Damage Mechanics Model for Ductile Fracture, *Journal of Engineering Materials and Technology* 107 (1) (1985) 83–89. doi:10.1115/1.3225775.
- [7] A. L. Gurson, Continuum theory of ductile rupture by void nucleation and growth: Part i—yield criteria and flow rules for porous ductile media, *Journal of Engineering Materials and Technology-transactions of The Asme* 99 (1977) 2–15. doi:10.1115/1.3443401.
- [8] J. Simo, J.-W. Ju, Strain- and stress-based continuum damage models. i. formulation, *International Journal of Solids and Structures* 23 (1987) 821–840. doi:10.1016/0020-7683(87)90083-7.
- [9] M. Brünig, An anisotropic ductile damage model based on irreversible thermodynamics, *International Journal of Plasticity* 19 (10) (2003) 1679–1713. doi:10.1016/S0749-6419(02)00114-6.
- [10] P. Steinmann, I. Carol, A framework for geometrically nonlinear continuum damage mechanics, *International Journal of Engineering Science* 36 (15) (1998) 1793–1814. doi:10.1016/S0020-7225(97)00116-X.
- [11] M. Ekh, A. Menzel, K. Runesson, P. Steinmann, Anisotropic damage with the mcr effect coupled to plasticity, *International Journal of Engineering Science* 41 (13) (2003) 1535–1551, damage and failure analysis of materials. doi:10.1016/S0020-7225(03)00032-6.
- [12] T. Wierzbicki, Y. Bao, Y. Bai, A New Experimental Technique for Constructing a Fracture Envelope of Metals under Multi-axial loading, *Proceedings of the 2005 SEM Annual Conference and Exposition on Experimental and Applied Mechanics* (2005).
- [13] Y. Bai, T. Wierzbicki, A new model of metal plasticity and fracture with pressure and lode dependence, *International Journal of Plasticity* 24 (6) (2008) 1071–1096. doi:10.1016/j.ijplas.2007.09.004.
- [14] F. A. McClintock, A Criterion for Ductile Fracture by the Growth of Holes, *Journal of Applied Mechanics* 35 (2) (1968) 363–371. doi:10.1115/1.3601204.
- [15] J. Rice, D. Tracey, On the ductile enlargement of voids in triaxial stress fields, *Journal of the Mechanics and Physics of Solids* 17 (3) (1969) 201–217. doi:10.1016/0022-5096(69)90033-7.
- [16] A. Mattiello, R. Desmorat, Lode angle dependency due to anisotropic damage, *International Journal of Damage Mechanics* 30 (2) (2021) 214–259. doi:10.1177/1056789520948563.
- [17] R. Gitschel, O. Hering, A. Schulze, A. Erman Tekkaya, Controlling Damage Evolution in Geometrically Identical Cold Forged Parts by Counterpressure, *Journal of Manufacturing Science and Engineering* 145 (1) (2023) 011011. doi:10.1115/1.4056266.
- [18] A. Menzel, M. Ekh, P. Steinmann, K. Runesson, Anisotropic damage coupled to plasticity: Modelling based on the effective configuration concept, *International Journal for Numerical Methods in Engineering* 54 (10) (2002) 1409–1430. doi:10.1002/nme.470.
- [19] J. Lemaitre, R. Desmorat, *Engineering Damage Mechanics. Ductile, Creep, Fatigue and Brittle Failure*, 2005. doi:10.1007/b138882.
- [20] A. E. Green, P. M. Naghdi, A general theory of an elastic-plastic continuum, *Archive for Rational Mechanics and Analysis* 18 (4) (1965) 251–281. doi:10.1007/BF00251666.
- [21] B. Halphen, Q. S. Nguyen, *Sur les matériaux standard généralisés*, 1975.
- [22] C. Frederick, P. Armstrong, A Mathematical Representation of the Multiaxial Bauschinger Effect, *Materials at High Temperatures* 24 (2007) 1–26. doi:10.3184/096034007X207589.
- [23] K. Langenfeld, A. Schowtjak, R. Schulte, O. Hering, K. Möhring, T. Clausmeyer, R. Ostwald, F. Walther, A. Tekkaya, J. Mosler, Influence of anisotropic damage evolution on cold forging, *Production Engineering* 14 (01 2020). doi:10.1007/s11740-019-00942-y.
- [24] K. Langenfeld, K. Möhring, F. Walther, J. Mosler, On the regularization for ductile damage models, *PAMM* 19 (1) (2019) e201900003. doi:10.1002/pamm.201900003.

- [25] K. Langenfeld, J. Mosler, A micromorphic approach for gradient-enhanced anisotropic ductile damage, *Computer Methods in Applied Mechanics and Engineering* 360 (2020) 112717. doi:10.1016/j.cma.2019.112717.
- [26] A. E. Tekkaya, N. Ben Khalifa, O. Hering, R. Meya, S. Myslicki, F. Walther, Forming-induced damage and its effects on product properties, *CIRP Annals* 66 (1) (2017) 281–284. doi:10.1016/j.cirp.2017.04.113.
- [27] F. X. C. Andrade, M. Feucht, A. Haufe, F. Neukamm, An incremental stress state dependent damage model for ductile failure prediction, *International Journal of Fracture* 200 (1-2) (2016) 127–150. doi:10.1007/s10704-016-0081-2.
- [28] J. Kennedy, R. Eberhart, Particle swarm optimization, in: *Proceedings of ICNN'95 - International Conference on Neural Networks*, Vol. 4, 1995, pp. 1942–1948 vol.4. doi:10.1109/ICNN.1995.488968.
- [29] J. A. Nelder, R. Mead, A simplex method for function minimization, *Comput. J.* 7 (1965) 308–313. doi:10.1093/comjnl/7.4.308.